***Manuscript submitted to Geophysical Journal International***

# Title: Analytical solution for the stress field in elastic half space with a spherical pressurized cavity or inclusion containing eigenstrain

*Xin, Zhong,* [1]*, Marcin, Dabrowski*[1,2]*, Bjørn Jamtveit*[1]

1. *Physics of Geological Processes, The Njord Center, University of Oslo, Norway*
2. *Computational Geology Laboratory, Polish Geological Institute - NRI, Wrocław, Poland*

*Contact author: Xin Zhong (xinzhong0708@gmail.com)*

## Summary

We present an analytical solution based on the series expansion of Papkovich-Boussinesq's displacement potentials to derive the elastic solution of a spherical inclusion containing an eigenstrain or pressurized cavity in an elastic half space. The inclusion-host interface can be treated as perfectly bonded or allowing different amount of interface sliding as a function of shear stress. The analytical solution allows systematic investigation on some key parameters that control the elastic stress field, such as inclusion depth, elastic moduli and the amount of interface sliding. The model is applied to study the distribution of stress and displacement within and around the inclusion. Stress trajectories and slip lines are computed around a pressurized cavity based on the analytical solution to study potential fracture modes and patterns. The amount of inclusion pressure relaxation due to the free surface is also systematically investigated as a function of inclusion depth and shear modulus ratio between the host and inclusion. A MATLAB code is provided that allows one to directly apply the analytical solution to natural systems given any elastic parameters. The code is benchmarked with Mindlin's solution for loaded homogeneous inclusion in proximity to a free surface and 3D finite element simulations for heterogeneous inclusion. This model may contribute to the study of the mechanical properties of natural systems at various scales, from *km* size magma chamber to *mm*-*μm* size mineral inclusions sealed in thin-section.


## Introduction

Natural systems are geometrically complicated but they may often be reduced to simpler setups as a first-order approximation. One common example is a system composed of a spherical inclusion embedded in a host material under various spatial scales, e.g. from *km* size magma chambers to *cm*-*mm* size porphyroblasts in rocks, down to even *μm*-*nm* size inclusions or impurities in a single crystal. When cooling/heating or phase transformation occurs, the volume of the inclusion and host do not necessarily vary homogeneously, thus stress variations are generated due to this differential expansion/contraction between the inclusion and host (Mura, 1987; Zhang, 1998). It has been known that the stress state within an ellipsoidal inclusion is homogeneous if the inclusion is surrounded by infinite host (Eshelby, 1957). However, when a free surface is present close to the inclusion, the stress becomes heterogeneous within the inclusion and is significant disturbed at the location between inclusion and free surface (e.g. Mindlin and Cheng, 1950; Seo and Mura, 1979). This situation is of significant importance in some geophysical and geological problems, e.g. investigations of the surface displacement and stress caused by a pressurized magma chamber (e.g. Browning and Gudmundsson, 2015; Galland et al., 2015; Gerbault et al., 2018; Guldstrand et al., 2018; Segall, 2005), or the residual pressure of mineral inclusion sealed in a thin-section (e.g. Enami et al., 2007; Kohn, 2014; Mazzucchelli et al., 2018; Thomas and Spear, 2018; Zhong et al., 2018). Relevant efforts in search of the elastic solution in half-space with different types of inclusion involve e.g. a loaded point source (Mogi, 1958), homogeneous cuboidal inclusion (the elastic moduli of inclusion is the same as the host) (Chiu, 1978) or pressurized horizontal circular crack (Fialko et al., 2001). Here, we present an analytical method that yields the stress field for a heterogeneous spherical inclusion or a pressurized cavity embedded in an elastic half-space. The method is based on the series expansion of Papkovich-Boussinesq's displacement potentials. It was developed to solve engineering problems such as stress analysis around a cavity or impurity (e.g. Kouris and Mura, 1989; Lee et al., 1992; Mi and Kouris, 2013, 2006; Mura et al., 1985; Tsuchida and Nakahara, 1970). Additionally, the inclusion-host interface can be treated as perfectly bonded or it can accommodate different amount of sliding due to the existing shear stress at the inclusion-host interface.

This paper has three folds: 1) Presenting the basic mathematical derivations of the analytical solution; 2) Providing a MATLAB code that allows simple applications of the analytical solution to different natural systems given elastic moduli and eigenstrain within inclusion or pressure within cavity. The MATLAB code has been validated against finite element (FE) solutions and Mindlin's analytical solution for an inclusion possessing the same elastic moduli as the host (Mindlin and Cheng, 1950); 3) Using the solution to systematically examine the effect of inclusion depth, interface sliding and elastic moduli on stress and displacement distributions in systems composed of host materials entrapping either an inclusion with eigenstrain or a pressurized cavity.

## Analytical solution for spherical inclusion in half-space

### Model setup

Consider a spherical inclusion (or cavity) is placed at the coordinate system origin as shown in Fig. 1. Apart from Cartesian reference system, both cylindrical and spherical reference systems are used in this work. For cylindrical reference system, the coordinates are $r, \theta, z$. For spherical reference system, the coordinates are $R, \theta, \phi$ (see Fig. 1). Due to the axial symmetry of the model geometry and the applied load, the solution is not dependent on coordinate $\theta$. For mathematical convenience the inclusion radius is set as one. The inclusion may possess different elastic moduli compared to the surrounding host. Both inclusion and host are elastically isotropic. The free surface is located at $z = -d$, where $d$ is the depth (Fig. 1). The remaining boundaries are considered to be infinitely far away from the inclusion. The depth $d$ needs to be higher than one so that the inclusion is not truncated by the free surface. Two types of inclusions are considered: 1) an inclusion subject to an isotropic eigenstrain that corresponds to the difference of volumetric strain between inclusion and host after e.g. temperature/pressure changes or phase transition (Mura, 1987); 2) a pressurized cavity containing a known pressure. The far-field confining pressure is set as zero.

## Host

We use the Papkovich-Boussinesq's displacement potentials to obtain the elastic solution. Any harmonic functions can be substituted into the potential representations, which are used to obtain stress and displacement that automatically satisfy the mechanical equilibrium requirement (see formulas in Appendix). For inclusion-host system, the displacement potentials are defined separately for inclusion and host. For the host, we introduce two sets of superimposed Papkovich-Boussinesq's displacement potentials expanded as infinite series or integrals of harmonic functions denoted by the Roman numbers as follow (see e.g. Tsuchida and Nakahara, 1970):

$$\begin{cases} \Phi_0^{\mathrm{I}} = 2Ge^* \sum_{n=0}^{N} A_n \frac{P_n(\mu)}{R^{n+1}} \\ \Phi_3^{\mathrm{I}} = 2Ge^* \sum_{n=0}^{N} B_n \frac{P_n(\mu)}{R^{n+1}} \end{cases} \tag{1}$$

$$\begin{cases} \Phi_0^{\mathrm{II}} = 2Ge^* \int_0^\infty \psi_1(\lambda) J_0(\lambda r) e^{-\lambda z} d\lambda \\ \Phi_3^{\mathrm{II}} = 2Ge^* \int_0^\infty \lambda \psi_2(\lambda) J_0(\lambda r) e^{-\lambda z} d\lambda \end{cases} \tag{2}$$

where $\mu = cos(\phi)$, $P_n(\mu)$ is the Legendre polynomial of order $n$, $J_0$ is the Bessel function of order zero, $A_n$, $B_n$ are the unknowns that control the elastic solution in the host, $G$ is the shear modulus of the host, $e^*$ is the eigenstrain of inclusion. In case of a pressurized cavity with pressure $P_{inc}$, the pre-factor $2Ge^*$ is replaced by $P_{inc}$. Both $\psi_1(\lambda)$ and $\psi_2(\lambda)$ are functions later determined by the unknowns $A_n$, $B_n$. The integer $N$ controls the order of truncation for the series, thus the accuracy of the solution.

The first set of potentials in Eq. 1 is defined in spherical reference system to describe the basic solution for a spherical inclusion in infinite host. The second set of potentials in Eq. 2 in cylindrical coordinate is introduced to impose corrections on Eq. 1 to satisfy the free surface conditions. For this purpose, the functions $\psi_1(\lambda)$ and $\psi_2(\lambda)$ are subsequently obtained based on the constraints of stress-free surface conditions.

These two sets of displacement potentials can be transformed between cylindrical reference system and spherical reference system as follow (see transformation relations in Appendix).

$$\begin{cases} \Phi_0^{\mathrm{I}} = 2Ge^* \sum_{n=0}^{N} A_n \frac{(-1)^n}{n!} \int_0^\infty \lambda^n J_0(\lambda r) e^{\lambda z} d\lambda \\ \Phi_3^{\mathrm{I}} = 2Ge^* \sum_{n=0}^{N} B_n \frac{(-1)^n}{n!} \int_0^\infty \lambda^n J_0(\lambda r) e^{\lambda z} d\lambda \end{cases} \quad (z \le 0) \tag{3}$$

$$\begin{cases} \Phi_0^{\mathrm{II}} = 2Ge^* \sum_{n=0}^{N} \int_0^\infty \psi_1(\lambda)(-1)^n \frac{(\lambda R)^n}{n!} P_n(\mu) d\lambda \\ \Phi_3^{\mathrm{II}} = 2Ge^* \sum_{n=0}^{N} \int_0^\infty \lambda \psi_2(\lambda)(-1)^n \frac{(\lambda R)^n}{n!} P_n(\mu) d\lambda \end{cases} \tag{4}$$

The potentials in Eq. 3 defined in cylindrical reference system are obtained from Eq. 1 in spherical reference system. The potentials in Eq. 4 in spherical reference system are obtained from Eq. 2 in cylindrical coordinate. The reason for introducing such coordinate transformation is due to the need of superposition (summation) of these two sets of displacement potential I and II to obtain the stress and displacement in spherical and cylindrical reference systems.

The free surface conditions are as follow:

$$\begin{aligned} &(1) \ \ \sigma_{zz}|_{z=-d} = 0 \\ &(2) \ \ \sigma_{rz}|_{z=-d} = 0 \end{aligned} \tag{5}$$

where $\sigma$ denotes stress tensor. The stresses $\sigma_{zz}$ and $\sigma_{rz}$ at $z = -d$ in the host can be expressed based on the displacement potentials $\Phi_0^{\mathrm{II}}$, $\Phi_3^{\mathrm{II}}$ in Eq. 2 and $\Phi_0^{\mathrm{I}}$, $\Phi_3^{\mathrm{I}}$ in Eq. 3 (see Appendix):

$$\sigma_{zz}|_{z=-d} = e^* \int_0^\infty \lambda \left\{ \lambda \psi_1(\lambda) e^{\lambda d} + \lambda(2 - 2\nu - \lambda d) e^{\lambda d} \psi_2(\lambda) + \sum_{n=0}^{N} \frac{(-1)^n}{n!} \lambda^n e^{-\lambda d} [\lambda A_n - (2 - 2\nu + \lambda d) B_n] \right\} J_0(\lambda r) d\lambda \tag{6}$$

$$\sigma_{rz}|_{z=-d} = e^* \int_0^\infty \lambda \left\{ \lambda \psi_1(\lambda) e^{\lambda d} + \lambda(1 - 2\nu - \lambda d) e^{\lambda d} \psi_2(\lambda) - \sum_{n=0}^{N} \frac{(-1)^n}{n!} \lambda^n e^{-\lambda d} [\lambda A_n - (1 - 2\nu + \lambda d) B_n] \right\} J_1(\lambda r) d\lambda \tag{7}$$

where $\nu$ is the Poisson ratio of the host. By letting the formula in curly brackets to be zero, $\sigma_{zz}$ and $\sigma_{rz}$ vanish at the surface. This leads to two equations with two unknown functions. Upon solving the system of equations, $\psi_1(\lambda)$ and $\psi_2(\lambda)$ are obtained.

$$\psi_1(\lambda) = e^{-2\lambda d} \sum_{m=0}^{N} \frac{(-1)^{m-1}}{m!} \lambda^{m-1} \{-(3 - 4\nu - 2\lambda d)\lambda A_m + [4(1-\nu)(1-2\nu) - 2\lambda^2 d^2] B_m\} \quad (8)$$

$$\psi_2(\lambda) = -e^{-2\lambda d} \sum_{m=0}^{N} \frac{(-1)^{m-1}}{m!} \lambda^{m-1} \{-2\lambda A_m + (3 - 4\nu + 2\lambda d) B_m\} \quad (9)$$

These two functions are substituted into the displacement potentials $\Phi_0^{\mathrm{II}}$ and $\Phi_3^{\mathrm{II}}$ in Eq. 4. After substitution, we obtain a set of displacement potentials:

$$\begin{cases} \Phi_0^{\mathrm{II}} = 2Ge^* \sum_{n=0}^{N} \alpha_n R^n P_n(\mu) \\ \Phi_3^{\mathrm{II}} = 2Ge^* \sum_{n=0}^{N} \beta_n R^n P_n(\mu) \end{cases} \quad (10)$$

where $\alpha_n$ and $\beta_n$ are as follow:

$$\alpha_n = \sum_{m=0}^{N} [\gamma_n^m (3 - 4\nu) + 2d\gamma_n^{m+1}(m+1)] A_m + \sum_{m=1}^{N} \left[4 \frac{\gamma_n^{m-1}}{m}(1-\nu)(1-2\nu) - 2d^2 \gamma_n^{m+1}(m+1)\right] B_m \quad (11)$$

$$\beta_n = \sum_{m=0}^{N} 2(m+1)\gamma_n^{m+1} A_m + [(3-4\nu)\gamma_n^m - 2d(m+1)\gamma_n^{m+1}] B_m$$

The shorthand notation $\gamma_n^m$ is defined as:

$$\gamma_n^m = \frac{(-1)^{n+m}}{m!\,n!} \int_0^\infty e^{-2\lambda} \lambda^{n+m} d\lambda = \frac{(-1)^{n+m}}{m!\,n!} \frac{(n+m)!}{(2d)^{n+m+1}} \quad (12)$$

Once $\alpha_n$ and $\beta_n$ are found out, we can substitute displacement potentials given in Eq. 1 and Eq. 10 into the following formulas representing displacement and stress (see Appendix). The displacement potentials I and II need to be superimposed.

$$2Gu_R = \frac{\partial \Phi_0}{\partial R} + \mu \left[R \frac{\partial \Phi_3}{\partial R} - (3-4\nu)\Phi_3\right]$$

$$2Gu_\phi = -\sin(\phi) \left[\frac{1}{R} \frac{\partial \Phi_0}{\partial \mu} + \mu \frac{\partial \Phi_3}{\partial \mu} - (3-4\nu)\Phi_3\right] \quad (13)$$

$$\sigma_{RR} = \frac{\partial^2 \Phi_0}{\partial R^2} + \mu R \frac{\partial^2 \Phi_3}{\partial R^2} - 2(1-\nu)\mu \frac{\partial \Phi_3}{\partial R} - 2\nu \frac{1-\mu^2}{R} \frac{\partial \Phi_3}{\partial \mu}$$

$$\sigma_{\phi R} = \sin\phi \left[\frac{1}{R^2} \frac{\partial \Phi_0}{\partial \mu} - \frac{1}{R} \frac{\partial^2 \Phi_0}{\partial \mu \partial R} + (1-2\nu)\frac{\partial \Phi_3}{\partial R} - \mu \frac{\partial^2 \Phi_3}{\partial \mu \partial R} + 2(1-\nu)\frac{\mu}{R}\frac{\partial \Phi_3}{\partial \mu}\right]$$

We can thus derive the stress and displacement at the inclusion-host interface ($R = 1$). For the displacement and stress of the host, we have the formula below. Some applied recurrence relations of Legendre polynomials for simplification purpose are provided in Appendix.

$$\frac{u_R}{e^*} = \sum_{n=0}^{N-1} \left[-(n+1)A_n + n\alpha_n - \frac{n^2 + n(3-4\nu)}{2n-1} B_{n-1} - \frac{(n+1)(n-4\nu+5)}{2n+3} B_{n+1} + \frac{n(n-4+4\nu)}{2n-1} \beta_{n-1} + \frac{(n+1)(n-2+4\nu)}{2n+3} \beta_{n+1}\right] P_n(\mu)$$

$$\frac{u_\phi}{e^* sin\phi} = -\sum_{n=1}^{N} \left[A_n + \alpha_n + \frac{n-4+4\nu}{2n-1} B_{n-1} + \frac{n+5-4\nu}{2n+3} B_{n+1} + \frac{n-4+4\nu}{2n-1} \beta_{n-1} + \frac{n+5-4\nu}{2n+3} \beta_{n+1}\right] P_n'(\mu)$$

$$\frac{\sigma_{RR}}{2Ge^*} = \sum_{n=0}^{N} \left[(n+1)(n+2)A_n + n(n-1)\alpha_n + \frac{n}{2n-1}(n^2 + 3n - 2\nu) B_{n-1} + \frac{(n+2)(n+1)(n+5-4\nu)}{2n+3} B_{n+1} + \right. \quad (14)$$

$$\frac{n(n-1)(n-4+4\nu)}{2n-1}\beta_{n-1} + \frac{(n+1)[n^2-2-n-2\nu]}{2n+3}\beta_{n+1}\Big] P_n(\mu)$$

$$\frac{1}{2Ge^*}\frac{\sigma_{R\phi}}{\sin\phi} = \sum_{n=1}^{N+1}\Big[(n+2)A_n - (n-1)\alpha_n + \frac{n^2-2+2\nu}{2n-1}B_{n-1} + \frac{(n+2)(n+5-4\nu)}{2n+3}B_{n+1} + \frac{(4-4\nu-n)(n-1)}{2n-1}\beta_{n-1} +$$
$$\frac{(-n^2+1-2n-2\nu)}{2n+3}\beta_{n+1}\Big] P_n'(\mu)$$

where $P_n'(\mu)$ is the derivative of Legendre polynomial with respect to $\mu$. The terms with subscript $n < 0$ or $n > N$ are not accounted for in the summation.

## Inclusion

Two types of inclusions are studied: 1) inclusion containing an eigenstrain; 2) pressurized cavity.

*Inclusion with eigenstrain*

For an inclusion with eigenstrain, we use the following displacement potentials in spherical coordinate (see Kouris and Mura, 1989):

$$\text{(III)}\begin{cases}\Phi_0 = 2\bar{G}e^*\sum_{n=0}^{N}\bar{A}_n P_n(\mu)R^n \\ \Phi_3 = 2\bar{G}e^*\sum_{n=0}^{N}\bar{B}_n P_n(\mu)R^n\end{cases} \tag{15}$$

where $\bar{A}_n$ and $\bar{B}_n$ are the unknowns describing the elastic solution in the inclusion. The overhead bar (e.g. $\bar{G}$) refers to the property of inclusion. This convention is used in the entire paper.

For inclusion, the stress and displacement can be obtained similarly to the host at $R = 1$:

$$\frac{\overline{u_R}}{e^*} = P_0(\mu) + \frac{G}{\bar{G}}\sum_{n=0}^{N-1}\Big[n\bar{A}_n + \frac{n(n-4+4\bar{\nu})}{2n-1}\bar{B}_{n-1} + \frac{(n+1)(n-2+4\bar{\nu})}{2n+3}\bar{B}_{n+1}\Big] P_n(\mu)$$

$$\frac{\overline{u_\phi}}{e^* sin\phi} = -\frac{G}{\bar{G}}\sum_{n=1}^{N}\Big[\bar{A}_n + \frac{n-4+4\bar{\nu}}{2n-1}\bar{B}_{n-1} + \frac{n+5-4\bar{\nu}}{2n+3}\bar{B}_{n+1}\Big] P_n'(\mu) \tag{16}$$

$$\frac{\overline{\sigma_{RR}}}{2Ge^*} = \sum_{n=0}^{N}\Big[n(n-1)\bar{A}_n + \frac{n(n-1)(n-4+4\bar{\nu})}{2n-1}\bar{B}_{n-1} + \frac{(n+1)[n^2-2-n-2\bar{\nu}]}{2n+3}\bar{B}_{n+1}\Big] P_n(\mu)$$

$$\frac{1}{2Ge^*}\frac{\overline{\sigma_{R\phi}}}{\sin\phi} = -\sum_{n=1}^{N+1}\Big[(n-1)\bar{A}_n + \frac{(n-1)(n-4+4\bar{\nu})}{2n-1}\bar{B}_{n-1} + \frac{(n^2-1+2n+2\bar{\nu})}{2n+3}\bar{B}_{n+1}\Big] P_n'(\mu)$$

The displacements at the centre point of the inclusion ($R = 0$) are expressed as follow:

$$\overline{u_R} = \frac{e^*G}{\bar{G}}[\bar{A}_1 + (-3+4\bar{\nu})\bar{B}_0]cos\phi \tag{17}$$

$$\overline{u_\phi} = -\frac{e^*G}{\bar{G}}[\bar{A}_1 + (-3+4\bar{\nu})\bar{B}_0]sin\phi$$

It is noted that $\overline{u_R}$ and $\overline{u_\phi}$ can be combined to generate a vertical displacement at the centre point of the inclusion: $u_z = \frac{e^*G}{\bar{G}}[\bar{A}_1 + (-3+4\bar{\nu})\bar{B}_0]$ . This contribution of vertical displacement is present within the inclusion regardless of $R$. Since $\bar{A}_1$ and $\bar{B}_0$ do not appear anywhere else in displacement or stress, only one of them needs to be constrained. Here, $\bar{B}_0$ is eliminated, and it is equivalent if one eliminates $\bar{A}_1$.

*Pressurized cavity*

A simpler scenario is when the inclusion is replaced by a cavity or any inclusion materials with very low shear modulus (e.g. hot magma in a magma chamber) and the pressure within the inclusion is prescribed by $P_{inc}$. The stress state at the inclusion-host interface on the inclusion side can be simplified as follow:

$$\begin{aligned} \overline{\sigma_{RR}} &= -P_{inc}\, P_0(\mu) \\ \overline{\sigma_{R\phi}} &= 0 \end{aligned} \tag{18}$$

It is noted that the unknowns $\bar{A}_n$ and $\bar{B}_n$ are not needed anymore. This is due to the homogeneous stress state within the inclusion as a consequence of zero shear modulus. It is noted that in the absence of eigenstrain within the inclusion, $e^*$ needs to be replaced by $\frac{P_{inc}}{2G}$ for the computation of stress in the host (Eq. 14).

## Obtaining the solutions

To match the traction and displacement at the inclusion-host interface, we need the following constraints:

$$\begin{aligned} &(1)\quad \sigma_{RR}|_{R=1} = \overline{\sigma_{RR}}|_{R=1} \\ &(2)\quad \sigma_{R\phi}|_{R=1} = \overline{\sigma_{R\phi}}|_{R=1} \\ &(3)\quad u_R|_{R=1} = \overline{u_R}|_{R=1} \\ &(4)\quad u_\phi|_{R=1} - \overline{u_\phi}|_{R=1} = \chi \frac{\sigma_{R\phi}|_{R=1}}{G} \end{aligned} \tag{19}$$

where $u$ denotes displacement. The constraints $(1)$ and $(2)$ are imposed to match the traction at the interface between inclusion and host. The constraints $(3)$ and $(4)$ enforce the continuity for radial displacement and allows one to choose the type of inclusion-host interface using the parameter $\chi$ (e.g. Kouris and Mura, 1989). Here, we scale $\sigma_{R\phi}|_{R=1}$ using the host's shear modulus $G$ to make $\chi$ dimensionless (displacement is scaled by the inclusion radius). Perfectly bonded inclusion-host interface is chosen by letting $\chi = 0$. The amount of inclusion-host interface sliding can be set via letting $\chi$ higher than zero. A free-sliding interface is given if $\chi$ approaches infinity or is a finite value that is large enough to generate negligible $\sigma_{R\phi}$ at the interface.

In case of inclusion with eigenstrain, we substitute the stress and displacement of host (Eq. 14) and inclusion (Eq. 16) at the interface into Eq. 19. Since $\bar{A}_0$ is not constrained in any of the above equations, it is eliminated from the unknowns. By equating the coefficients of these four equations for the same order of $P_n(\mu)$ and $P_n'(\mu)$, we get $4N+2$ equations. Meanwhile, the number of unknowns is $4N+2$ including $A_{0\sim N}$, $B_{0\sim N}$, $\bar{A}_{1\sim N}$ and $\bar{B}_{1\sim \mathrm{N}}$. We can solve the system of equations to obtain all the unknowns that can be used to evaluate displacement and stress at different localities.

Similarly, in case of a pressurized cavity, we substitute the stress of the host (Eq. 14) and inclusion (Eq. 18) into (1-2) in Eq. 19 to match the traction at the interface. The unknowns are $A_{0\sim N}$, $B_{0\sim N}$ that can be solved based on the system of equations. In this case, the number of equations and the number of unknowns are both $2N+2$.

## Evaluating stress and displacement

In order to evaluate the stress and displacement for the host, we first substitute $\psi_1(\lambda)$ and $\psi_2(\lambda)$ (Eq. 8, 9) into displacement potentials $\Phi_0^{\mathrm{II}}$ and $\Phi_3^{\mathrm{II}}$ in Eq. 2, and subsequently apply the results together with $\Phi_0^{\mathrm{II}}$ and $\Phi_3^{\mathrm{II}}$ in Eq. 3 into the formulas giving stress and displacement in cylindrical coordinate (see Appendix). The integral involving Bessel function can be expressed by the following relation (Tsuchida and Nakahara, 1970):

$$\int_0^\infty J_i(\lambda r)e^{-a\lambda}\lambda^j d\lambda = (-1)^i \frac{(j-i)!}{(r^2+a^2)^{\frac{j+1}{2}}} P_j^i\left(\frac{a}{\sqrt{r^2+a^2}}\right) \tag{20}$$

where $P_j^i\left(\frac{a}{\sqrt{r^2+a^2}}\right)$ is the associated Legendre polynomials. The derived stress and displacement fields are as follow for the host:

$$u_r = e^* \sum_{n=0}^{N} (-1)^n \left\{-4B_n(2\nu-1)(\nu-1)\frac{P_n^1(\mu_0)}{nR_0^{n+1}} - (B_n z + A_n)(4\nu-3)\frac{P_{n+1}^1(\mu_0)}{R_0^{n+2}} + (B_n z + A_n)\frac{P_{n+1}^1(\mu_1)}{R_1^{n+2}} + 2(B_n d - A_n)(d+z)(n+1)\frac{P_{n+2}^1(\mu_0)}{R_0^{n+3}}\right\}$$

$$u_z = e^* \sum_{n=0}^{N} (-1)^n \left\{-2(n+2)(n+1)(B_n d - A_n)(d+z)\frac{P_{n+2}^0(\mu_0)}{R_0^{n+3}} + (4\nu-3)(n+1)[B_n(2d+z) - A_n]\frac{P_{n+1}^0(\mu_0)}{R_0^{n+2}} - (8\nu^2-12\nu+5)B_n\frac{P_n^0(\mu_0)}{R_0^{n+1}} + (B_n z + A_n)(n+1)\frac{P_{n+1}^0(\mu_1)}{R_1^{n+2}} + (4\nu-3)B_n\frac{P_n^0(\mu_1)}{R_1^{n+1}}\right\}$$

$$\frac{\sigma_{rr}}{2Ge^*} = \sum_{n=0}^{N} (-1)^n \left\{-2B_n(3\nu-2)(n+1)\frac{P_{n+1}^0(\mu_0)}{R_0^{n+2}} - 2B_n\nu(n+1)\frac{P_{n+1}^0(\mu_1)}{R_1^{n+2}} + (n+1)(n+\right.$$

$$2)[4B_n(d+z)\nu - 3zB_n - 3A_n]\frac{P^0_{n+2}(\mu_0)}{R_0^{n+3}} - (n+2)(n+1)(B_nz + A_n)\frac{P^0_{n+2}(\mu_1)}{R_1^{n+3}} - 2(n+1)(n+2)(n+3)(B_nz - A_n)(d+z)\frac{P^0_{n+3}(\mu_0)}{R_0^{n+4}} + 4B_n(\nu-1)(2\nu-1)\frac{P^1_n(\mu_0)}{nrR_0^{n+1}} + (B_nz + A_n)(4\nu-3)\frac{P^1_{n+1}(\mu_0)}{rR_0^{n+2}} - (B_nz + A_n)\frac{P^1_{n+1}(\mu_1)}{rR_1^{n+2}} - 2(n+1)(B_nd - A_n)(d+z)\frac{P^1_{n+2}(\mu_0)}{rR_0^{n+3}}\Big\} \quad (21)$$

$$\frac{\sigma_{zz}}{2Ge^*} = \sum_{n=0}^{N}(-1)^n\Big\{-2(\mathrm{n}+1)B_n(\nu-1)\frac{P^0_{n+1}(\mu_0)}{R_0^{n+2}} + 2(n+1)B_n(\nu-1)\frac{P^0_{n+1}(\mu_1)}{R_1^{n+2}} - (n+1)(n+2)[4(\nu-1)dB_n + (4\nu-3)zB_n + A_n]\frac{P^0_{n+2}(\mu_0)}{R_0^{n+3}} + (n+1)(n+2)(B_nz + A_n)\frac{P^0_{n+2}(\mu_1)}{R_1^{n+3}} + 2(n+1)(n+2)(n+3)(B_nd - A_n)(d+z)\frac{P^0_{n+3}(\mu_0)}{R_0^{n+4}}\Big\}$$

$$\frac{\sigma_{rz}}{2Ge^*} = \sum_{n=0}^{N}(-1)^n\Big\{-B_n(2\nu-1)\frac{P^1_{n+1}(\mu_0)}{R_0^{n+2}} - 2(n+1)(n+2)(B_nd - A_n)(d+z)\frac{P^1_{n+3}(\mu_0)}{R_0^{n+4}} + (n+1)[4(d+z)\nu B_n - 2dB_n - 3zB_n - A_n]\frac{P^1_{n+2}(\mu_0)}{R_0^{n+3}} + (n+1)(B_nz + A_n)\frac{P^1_{n+2}(\mu_1)}{R_1^{n+3}} + B_n(2\nu-1)\frac{P^1_{n+1}(\mu_1)}{R_1^{n+2}}\Big\}$$

$$\frac{\sigma_{\theta\theta}}{2Ge^*} = \sum_{n=0}^{N}(-1)^n\Big\{-2(4\nu-3)B_n\nu(n+1)\frac{P^0_{n+1}(\mu_0)}{R_0^{n+2}} - 2B_n\nu(n+1)\frac{P^0_{n+1}(\mu_1)}{R_1^{n+2}} + 4\nu(n+1)(n+2)(B_nd - A_n)\frac{P^0_{n+2}(\mu_0)}{R_0^{n+3}} - 4B_n(\nu-1)(2\nu-1)\frac{P^1_n(\mu_0)}{nrR_0^{n+1}} - (4\nu-3)(B_nz + A_n)\frac{P^1_{n+1}(\mu_0)}{rR_0^{n+2}} + (B_nz + A_n)\frac{P^1_{n+1}(\mu_1)}{rR_1^{n+2}} + 2(n+1)(d+z)(B_nd - A_n)\frac{P^1_{n+2}(\mu_0)}{rR_0^{n+3}}\Big\}$$

where $P_n^0(\mu_0)$ is equivalent to the Legendre polynomial $P_n(\mu_0)$ used in the text. The following shorthand notations are used:

$$R_0 = \sqrt{(2d+z)^2 + r^2}$$
$$R_1 = \sqrt{z^2 + r^2} \quad (22)$$
$$\mu_0 = (z+2d)/R_0$$
$$\mu_1 = -z/R_1$$

Similarly, for the inclusion, the displacement and stress fields are expressed in spherical coordinate:

$$u_R = e^*R + \sum_{n=0}^{N}\frac{e^*P_n(\mu)}{\bar{G}}[\overline{A_n}nR^{n-1} + \overline{B_n}\mu(n+4\bar{\nu}-3)R^n]$$

$$u_\phi = -\sum_{n=0}^{N}\frac{e^*\sin(\phi)}{\bar{G}}\{\overline{A_n}P_n'(\mu)R^{n-1} + \overline{B_n}R^n[P_n'(\mu)\mu + (4\bar{\nu}-3)P_n(\mu)]\}$$

$$\frac{\sigma_{RR}}{2Ge^*} = \sum_{n=0}^{N}[\overline{A_n}R^{n-2}n(n-1) + \overline{B_n}R^{n-1}n\mu(n+2\bar{\nu}-3)]P_n(\mu) + 2\overline{B_n}R^{n-1}(\mu^2-1)\bar{\nu}P_n'(\mu) \quad (23)$$

$$\frac{\sigma_{\theta\theta}}{2Ge^*} = \sum_{n=0}^{N}[\overline{A_n}R^{n-2}n - \overline{B_n}R^{n-1}n\mu(2\bar{\nu}-1)]P_n(\mu) + [-\overline{A_n}\mu R^{n-2} + \overline{B_n}(2\bar{\nu}\mu^2 - \mu^2 - 2\bar{\nu})R^{n-1}]P_n'(\mu)$$

$$\frac{\sigma_{\phi\phi}}{2Ge^*} = \sum_{n=0}^{N}[-\overline{A_n}R^{n-2}n^2 - \overline{B_n}R^{n-1}n\mu(n+2\bar{\nu})]P_n(\mu) + [\overline{A_n}\mu R^{n-2} - \overline{B_n}(2\bar{\nu}\mu^2 - 3\mu^2 - 2\bar{\nu} + 2)R^{n-1}]P_n'(\mu)$$

$$\frac{\sigma_{R\phi}}{2Ge^*} = \sin(\phi)\sum_{n=0}^{N}(1-2\bar{\nu})n\overline{B_n}R^{n-1}P_n(\mu) + [-\overline{A_n}(n-1)R^{n-2} - \overline{B_n}\mu(n+2\bar{\nu}-2)R^{n-1}]P_n'(\mu)$$

Given the already obtained $A_n$, $B_n$, $\bar{A}_n$ and $\bar{B}_n$ (for pressurized cavity only $A_n$ and $B_n$), we can calculate all the stress and displacement components in both inclusion and host using the above functions.

## Model validation

The presented analytical solution is validated against the analytical solution of Mindlin and Cheng (1950) considering the inclusion to possess the same elastic moduli. The stress field is generated due to an eigenstrain within the inclusion. Both inclusion and host have a Poisson ratio of 0.25 and shear modulus of 1. The free surface is at $d = 1.5$, and the eigenstrain is 1. Perfectly bonded inclusion-host interface is applied by letting $\chi = 0$. The results are shown in Fig. 2.

In Fig. 3, the computed stresses are compared to the exact analytical solution from Mindlin and Cheng (1950) to investigate the effect of truncation number $N$ and inclusion depth on the computational error. The elastic parameters are the same as in Fig. 2. The error is quantified by the value $|\sigma^{Mindlin} - \sigma^{Series}|$, where $\sigma^{Mindlin}$ is the exact solution based on Mindlin and Cheng (1950), and $\sigma^{Series}$ is the computed result from this study. It is clear that the series expansion method provides sufficiently accurate solution, ca. $10^{-5}$ error, for the stress given $N > 20$ and $d > 1.2$. It is also noted that as inclusion depth increases, the required $N$ dramatically decreases.

Additionally, we perform 3D FE simulations using the code developed from Milamin (Dabrowski et al., 2008) to test the case for heterogeneous inclusion, i.e. the inclusion contains different elastic moduli than the host. Several sets of simulations involving different elastic moduli for inclusion and host have been performed. An example is shown in Fig. 4. The shear modulus of inclusion and host are 3 and 1, respectively. The Poisson ratio of inclusion and host are 0.25 and 0.35. The inclusion depth is 1.5. The match between the analytical solution and FE solutions confirms that the analytical solution can produce correct results for the case of heterogeneous inclusion. Similar level of match between the analytical and numerical solution is also obtained for the pressurized cavity case given different host Poisson ratio in a wide range.

## Results

### Pressurized cavity

We first focus on the effect of a pressurized cavity with $P_{inc}$ on the displacement and stress at the free surface. The cavity depth and Poisson ratio of the host are systematically varied to see how they affect the magnitude and distribution of displacement and stress on the free surface. Stresses $\sigma_{rr}$ and $\sigma_{\theta\theta}$ scaled by cavity pressure $P_{inc}$ are plotted in Fig. 5. It is shown that as inclusion depth increases (Fig. 5A and 5B), both $\sigma_{rr}$ and $\sigma_{\theta\theta}$ decrease. The decrease of the absolute value for stress is more significant when the cavity is close to the free surface. It is noted that when the cavity is close to the free surface ($d < 1.5$), negative $\sigma_{rr}$ is present at the surface at the distance greater than 0.7 to 1.1 from the centre of the surface (*r*=0) (Fig. 5A). This shows that compression is present in radial direction. This observation of negative $\sigma_{rr}$ is not significant when $d > 2$. The tangential stress $\sigma_{\theta\theta}$ is always positive, implying that extension in tangential direction is present given any cavity depth. When the Poisson ratio of the host decreases from 0.45 to 0.05 (Fig. 5C and 5D), overall $\sigma_{rr}$ decreases and $\sigma_{\theta\theta}$ decreases close to the centre (*r*=0).

The effect of cavity depth and host Poisson ratio on surface displacement is shown in Fig. 6. The displacement is scaled by a factor of cavity pressure $P_{inc}$ divided by host shear modulus $G$. It is noted that as the cavity depth increases, the overall radial displacement $u_r$ and vertical displacement $u_z$ decrease. When the cavity depth approaches 5, both radial and vertical displacements become relatively homogeneous. The peak radial displacement $u_r$ at the surface is shifted towards higher distance from the centre point as cavity depth increases (Fig. 6A). As host Poisson ratio decreases, the absolute value of radial and vertical displacement increases.

To better demonstrate the effect of pressurized cavity depth on the stress at the free surface, $\sigma_{rr}$ at the centre point of the free surface is plotted as a function of cavity depth given different Poisson ratio (Fig. 7). In this case, $\sigma_{rr}$ is equal to $\sigma_{\theta\theta}$ at the centre point of the free surface. It is shown that $\sigma_{rr}$ dramatically increase when the cavity depth is lower than 2, and drops below 0.1 when the cavity depth exceeds 3~4. As the host Poisson ratio decreases, the peak $\sigma_{rr}$ decreases at the centre point of free surface.

The stress trajectories for principle stresses and slip lines are shown in Fig. 8. The results are given for *x*-*z* plane. The host Poisson ratio is 0.3. The cavity depth is 1.5. Stress trajectories are computed based on the orientations of the maximal and minimal principle stresses in the

2D plane. In Fig. 8A, the background colour shows the magnitude of maximal principle stress. The white contours show the stress trajectories of maximal principle stress, and the black contours show the stress trajectories of minimal principle stress. If positive $P_{inc}$ is imposed in the cavity, mode I radial fractures may occur following the black contours. If negative $P_{inc}$ is imposed, mode I circular fractures may occur following the white contours. In Fig. 8B, the second invariant of stress tensor is plotted as background colour. The black contours are slip lines where mode II in-plane fractures may occur. The internal friction angle is set as $30^{o}$.

## Inclusion-host interface sliding

Different from the previously studied pressurized cavity case, an inclusion with eigenstrain may cause sliding at the inclusion-host interface. By varying the dimensionless parameter $\chi$, it is possible to systematically investigate the amount and effect of inclusion-host interface sliding. Fig. 9 shows the displacement and shear stress plotted along the inclusion-host interface. In this example, both inclusion and host possess Poisson ratio 0.3 and shear modulus ratio is one. The goal is to investigate how $\chi$ influences the displacement and stress.

It is found that by gradually increasing $\chi$, the tangential displacements of inclusion and host start to diverge, especially on the inclusion side. The maximal displacement mismatch occurs at the tangential angle ca. $\phi = 90{\sim}120°$. As a consequence of increasing the amount of interface sliding, the shear stress at the interface gradually relaxes until completely vanished when $\chi > 1000$.

The effect of inclusion depth on the amount of inclusion-host interface sliding is illustrated in Fig. 10. The black curve shows the case for perfectly bonded interface. Therefore, the tangential displacement $u_{\phi}$ is equal between inclusion and host. It is shown that when free sliding interface is imposed, $u_{\phi}$ at the inclusion side significantly diverge from the perfectly bonded case at inclusion depth $d$<2. When the inclusion depth is higher than 3, these two end members become similar. This suggests that the interface sliding effect is not negligible at shallower inclusion depth *d<2*~3.

## Inclusion pressure relaxation

Pressure relaxation occurs due to the proximity of inclusion to free surface. Apart from the inclusion depth, the elastic stiffness of the host also controls the amount of pressure relaxation.

Here, these two variables are systematically investigated: i.e. the inclusion depth, and shear modulus ratio. The Poisson ratio of both inclusion and host is set as 0.3. The pressures at four locations within the inclusion are shown in Fig. 11. The plotted pressure is scaled based on the expected inclusion pressure in infinite host as follow (simplified based on Eq. 22 in Zhang, 1998). Therefore, the dimensionless pressure is a value smaller than one that allows straightforward investigation on the relative amount of pressure relaxation.

$$P_{inc}^{exp} = 3e^*/(\frac{1}{\bar{K}} + \frac{3}{4G}) \tag{24}$$

In Fig. 11, the entrance of 3% pressure relaxation is illustrated with white contours. This amount of relaxed pressure is considered here as a small value. In general, elastically softer host crystal leads to higher amount of pressure relaxation, especially when the inclusion is close to free surface. The effect of inclusion-host interface sliding can be observed by comparing C and D in Fig. 11. In general, the effect is significant on the locations close to the inclusion-host interface (locations A, C and D), and much less significant at the inclusion centre (location B). For location A (inclusion top), negative pressure (extension) is observed when the depth is shallow and the surrounding host is elastically soft in the case of perfectly bonded inclusion-host interface. However, this is not observed for the free sliding case. The bottom of the inclusion (location C) undergoes significant amount of pressure relaxation in case of free sliding interface compared to perfectly bonded interface.

## Discussion and Conclusions

We present an analytical solution for the stress and displacement fields of systems composed of a spherical inclusion or a pressurized cavity in proximity to a free surface. The analytical solution is versatile in solving the elastic problem given any elastic stiffness of the system. The solution can be useful in studying problems such as surface stress and displacement above a pressurized magma chamber, or mineral inclusion containing residual pressure sealed in a thin-section. Using the derived analytical solution, we systematically investigate the dimensionless stress and displacement at the free surface above a pressurized cavity. Given the obtained stress tensor from analytical solution, stress trajectories and slip lines can also be visualized that provide insights on the potential mode and pattern of fractures.

The amount of pressure relaxation due to free surface is most significant under following scenarios: 1) when the measurements are performed at the top of the inclusion, 2) when the host is elastically soft. The difference of the inclusion's pressure variations between perfectly bonded and sliding interface can be significant. It needs to be highlighted that the bottom point of the inclusion undergoes significant pressure relaxation if interface sliding occurs. This is counter-intuitive and contrary than the perfectly bonded interface where the bottom point undergoes least pressure relaxation.

In general, the presented analytical solution has several potentials and implications:

- The analytical solution can be used for the verification of numerical codes for solving linear elastic problems based on e.g. finite element or finite difference methods etc.
- The stress and displacement field in an inclusion-host system can be investigated precisely at particular points that may be difficult to be approximated using numerical methods, e.g. along the interface or at the free surface.
- The effects of some key parameters in the studies of inclusion-host system, e.g. elastic moduli, inclusion depth from free surface, the sliding of inclusion-host interface etc. can be directly tested analytically.

The source code is available as executable MATLAB script in the supplementary material or upon personal request.


## Acknowledgements

This project has been supported by Swiss National Science Foundation (P2EZP2_172220) to XZ, and the European Union's Horizon 2020 Research and Innovation Programme under the ERC Advanced Grant Agreement n°669972, 'Disequilibrium Metamorphism' ('DIME') to BJ. MD acknowledges PGI-NRI project no. 61-9015-1601-00-0.

**Figures**

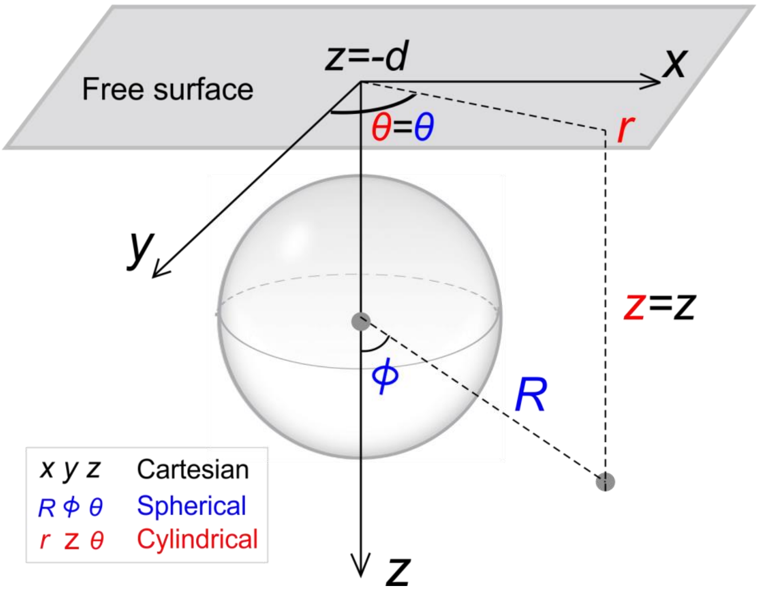


Fig. 1. A spherical inclusion close to free surface. The Cartesian, spherical and cylindrical coordinates are schematically shown using different colours. The inclusion radius is set as one. The free surface is located at $z = -d$.

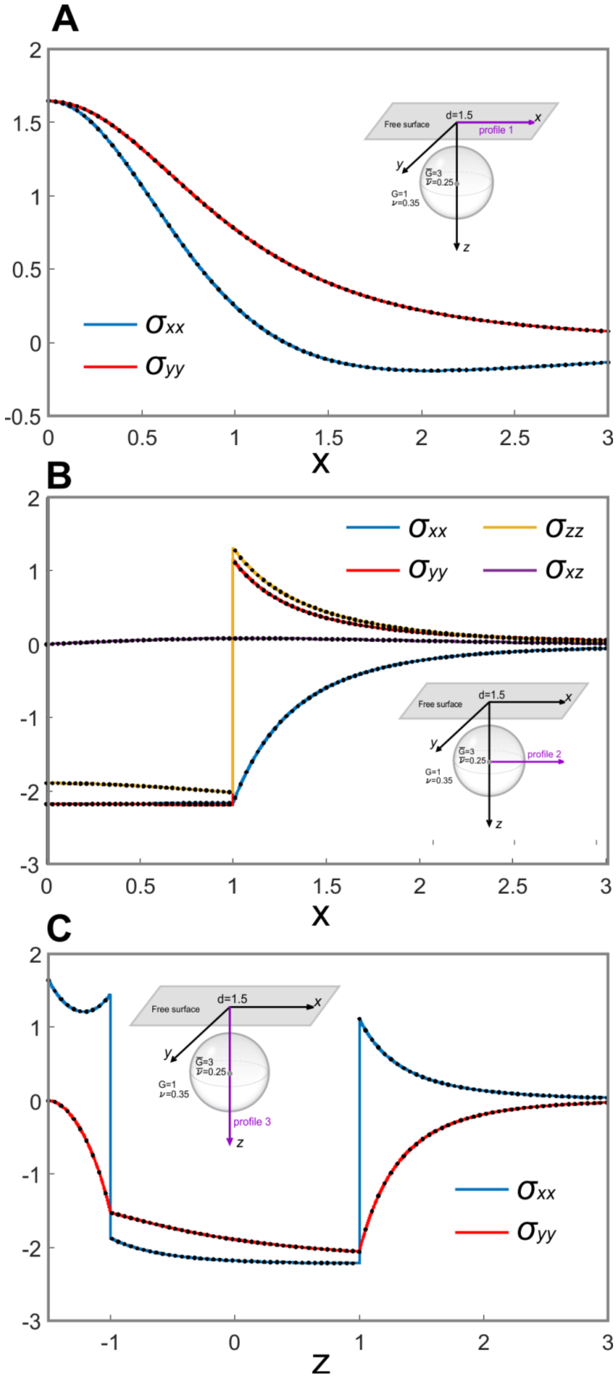


Fig. 2 Model benchmark results using Mindlin's solution in half space (curves) with depth 1.5 and this method (dots) given the same depth (Mindlin and Cheng, 1950). **A**, **B** and **C** show the stresses computed along the profiles denoted by the purple lines in each figure. Both inclusion and host have a Poisson ratio of 0.25 and shear modulus of 1. The number of displacement potential series *N* is chosen as 25.

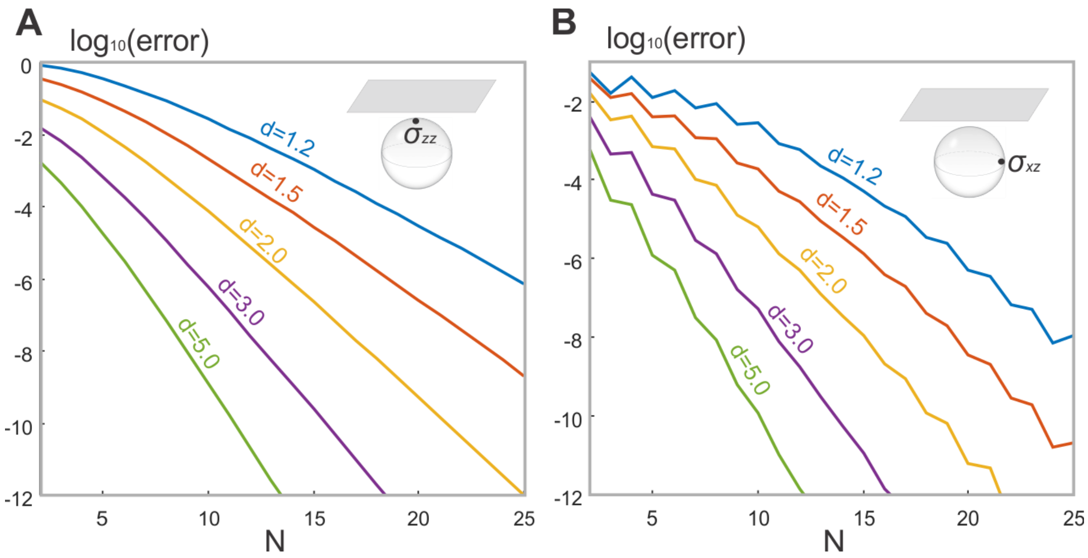


Fig. 3. Accuracy test showing the effect of $N$ on computed error at different inclusion depth. **A** is for the normal stress $\sigma_{zz}$ at the top point of inclusion, **B** is for the shear stress $\sigma_{xz}$ at the lateral point of inclusion. For **A**, the error is represented by $|\sigma_{zz}^{Mindlin} - \sigma_{zz}^{series}|$, where $\sigma_{zz}^{Mindlin}$ denotes the exact solution from Mindlin and Cheng, (1950) and $\sigma_{zz}^{series}$ denotes the series expansion solutions presented in this paper. The elastic moduli are the same as in Fig. 2.

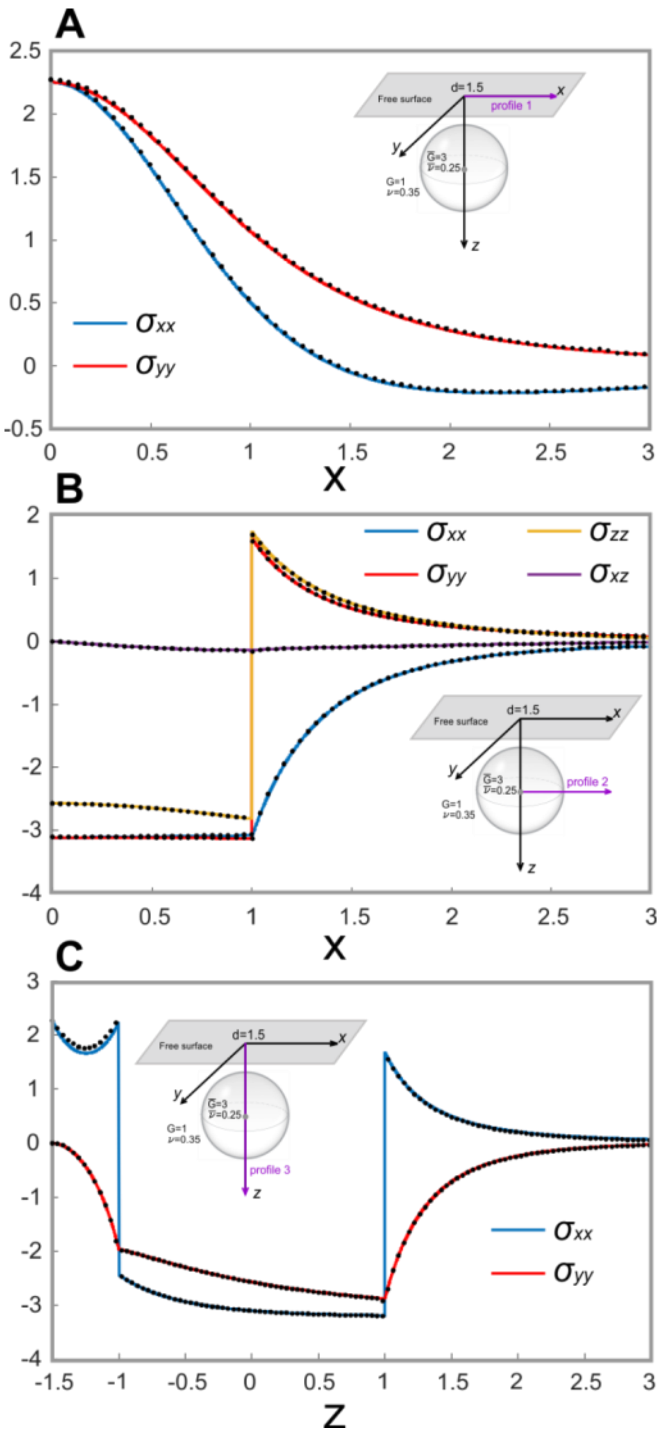


Fig. 4. Model benchmark results with FE solutions (dots). **A**, **B** and **C** show the stresses computed along the profiles denoted by the purple lines in each figure. The shear modulus of inclusion and host are 3 and 1, respectively. The Poisson ratio of the inclusion and host are 0.25 and 0.35. The inclusion depth is 1.5 and eigenstrain is 1. The number of displacement potential series $N$ is chosen as 25.

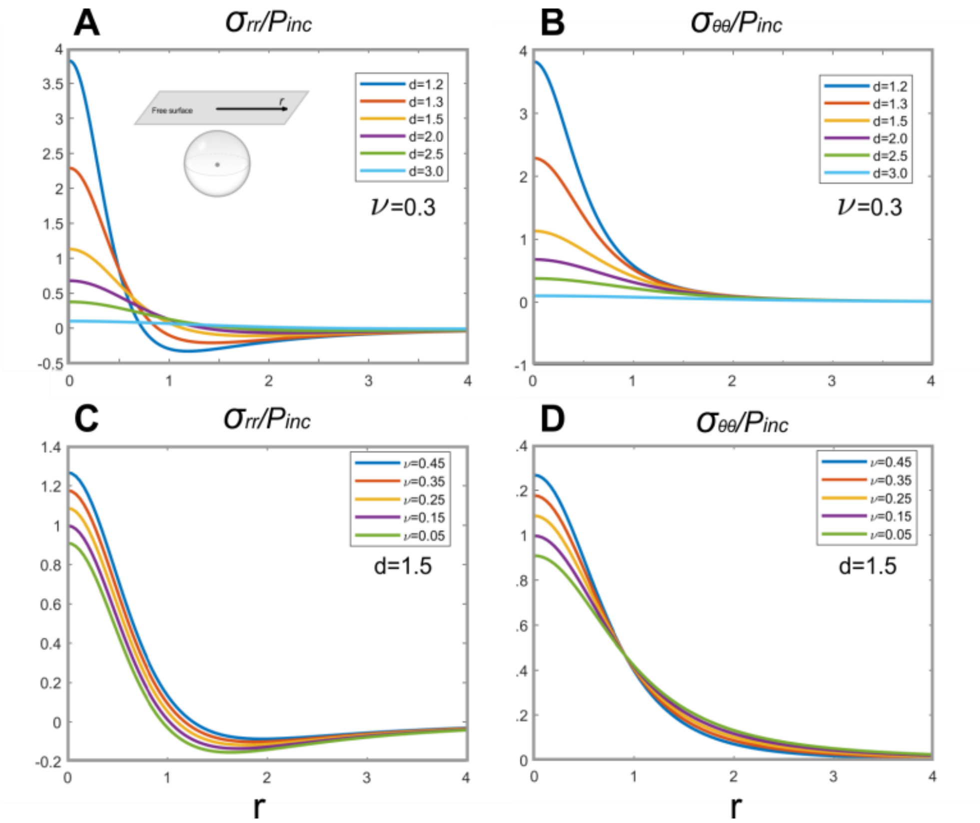


Fig. 5. Computed $\sigma_{rr}$ and $\sigma_{\theta\theta}$ along $r$ direction at the surface above a cavity with pressure $P_{inc}$. **A** and **B** are plotted stresses as a function of cavity depth given same Poisson ratio. **C** and **D** are plotted stresses as a function of Poisson ratio given the same cavity depth. The stresses are scaled by $P_{inc}$.

395

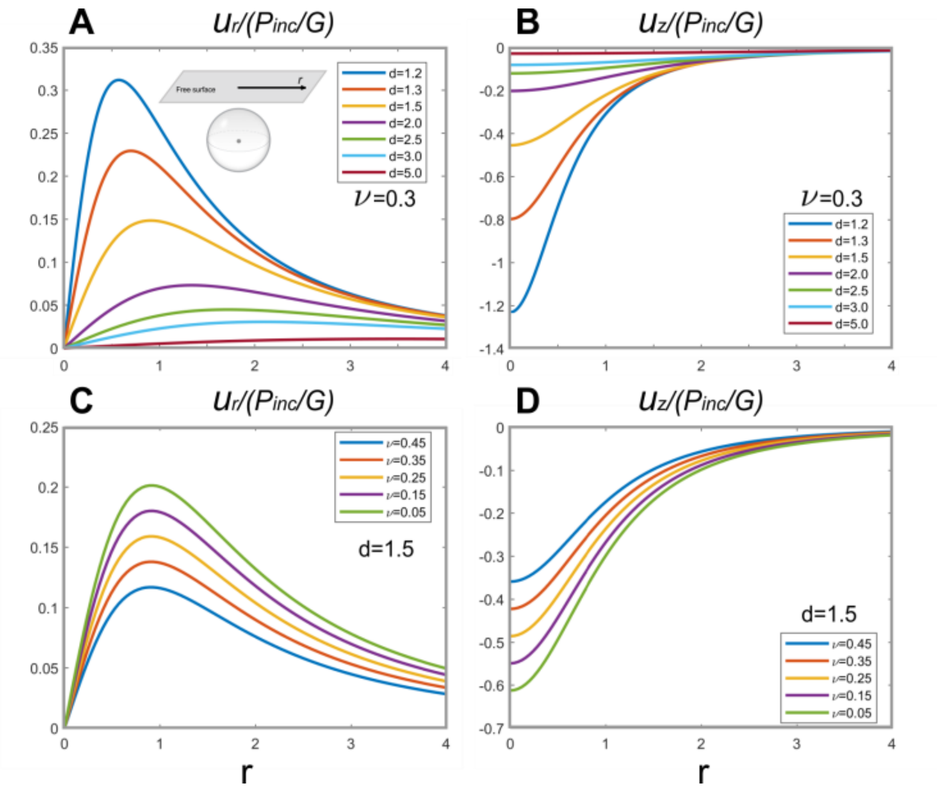


396 Fig. 6. Computed $u_r$ and $u_z$ along $x$ direction at the surface above a cavity with pressure $P_{inc}$.
397 **A** and **B** show plotted displacements as a function of cavity depth given the same Poisson
398 ratio. **C** and **D** show plotted displacements as a function of Poisson ratio at the same depth.
399 The displacements are scaled based on cavity pressure and shear modulus of the host.

400

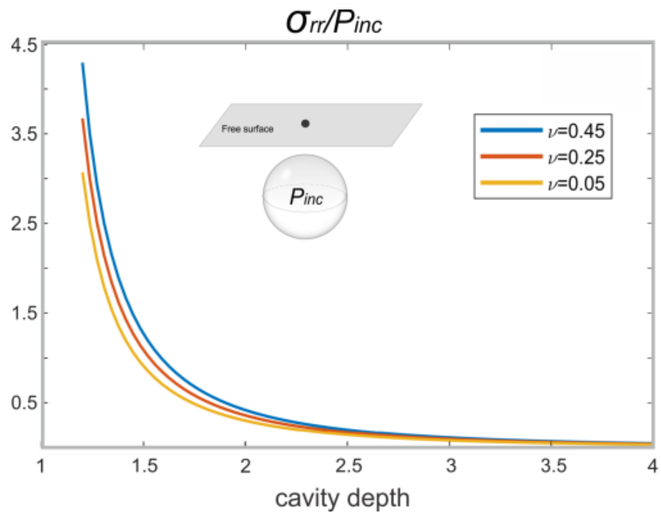


Fig. 7. Plotted $\sigma_{rr}$ as a function of pressurized cavity depth evaluated at the centre point of free surface shown by the black dot in the small figure. The host Poisson ratio are denoted by different colour.

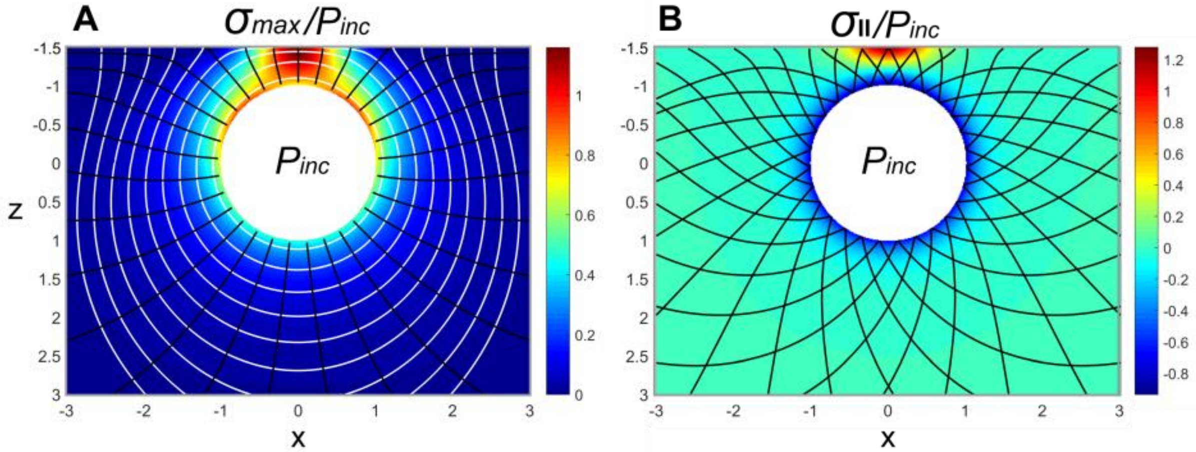


Fig. 8. Computed maximal principle stress in **A** and the second invariant of stress tensor in **B** around a pressurized cavity $P_{inc}$. In **A**, the stress trajectories for the maximal principle stress are shown by white contours and the minimal principle stress by black contours. Mode I radial fractures may occur following the black contours given positive $P_{inc}$. In **B**, slip lines are shown by black contours. Mode II fractures may occur following the black contours. The internal friction angle is $30^{o}$. The host Poisson ratio is 0.3. The cavity depth is 1.5.

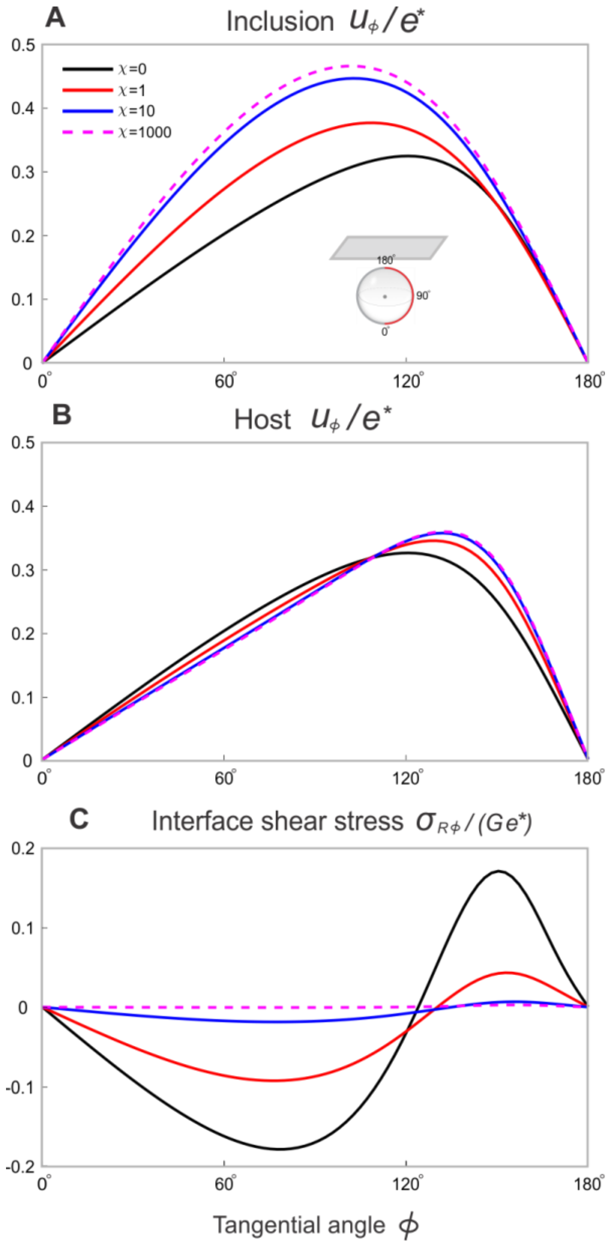


Fig. 9. Tangential displacement and shear stress plotted along the inclusion-host interface with different $\chi$. The inclusion and host possess Poisson ratio 0.3. The displacements on both sides of host and inclusion overlap when $\chi = 0$ for perfectly bonded case and diverge when $\chi > 0$. The inclusion depth is set as 1.2.

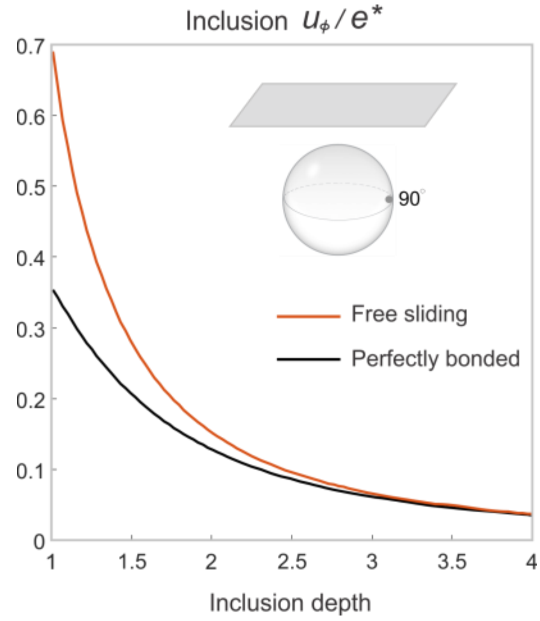


Fig. 10. Effect of inclusion depth on the amount of interface sliding. The shear modulus ratio is set as one. The tangential displacement $u_\phi$ is taken at the locality shown by the grey dot on the inclusion. The parameter $\chi$ is set as 10000 to guarantee free sliding. The inclusion and host have Poisson ratio 0.3.

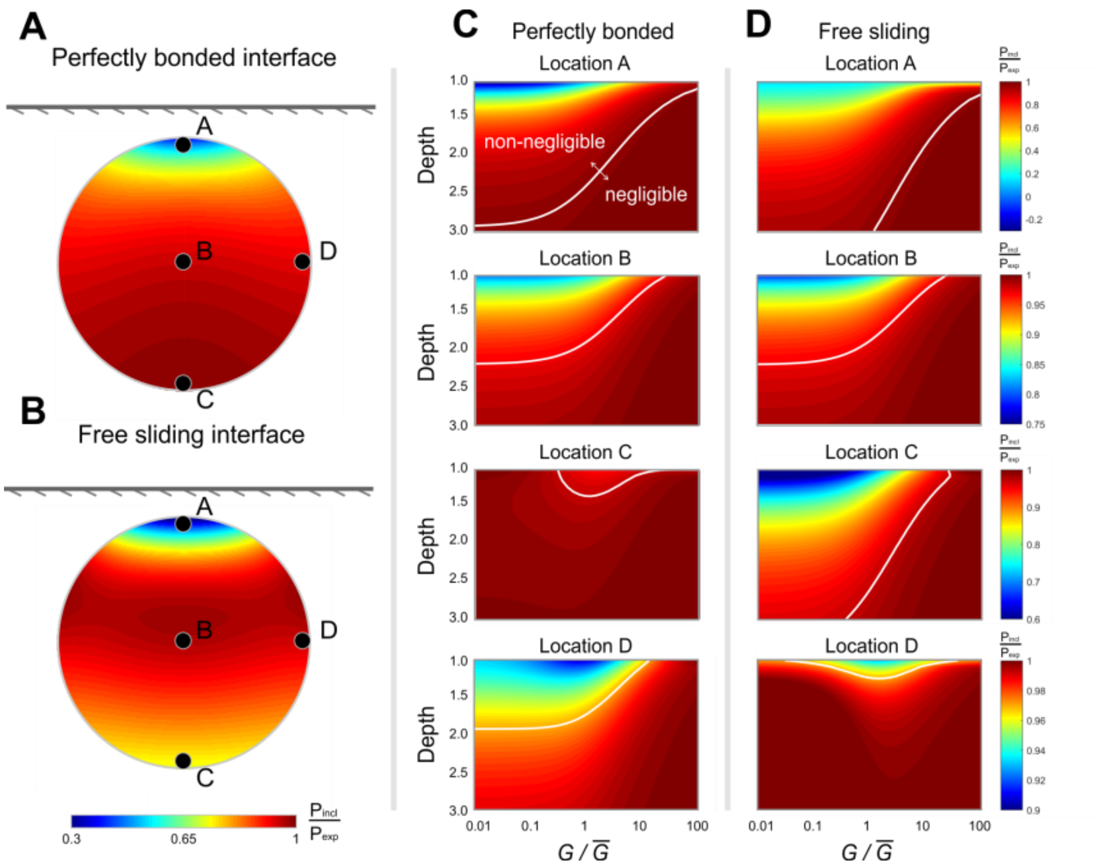


Fig. 11. **A-B** show the pressure variations within inclusion at depth 1.2. Pressure is scaled based on the expected pressure assuming infinite host radius. The shear modulus ratio is one. The Poisson ratios of inclusion and host are set as 0.3. **C-D** show the pressure measured at four locations denoted in **A** and **B** as a function of inclusion depth and shear modulus ratio. **A** and **C** are for perfectly bonded inclusion-host interface, **B** and **D** are for free sliding case ($\chi = 10^5$). The white contours in **C-D** show the entrances of 3% pressure relaxation compared to the expected value in infinite host.

## References


Browning, J., Gudmundsson, A., 2015. Surface displacements resulting from magma-chamber roof subsidence, with application to the 2014-2015 Bardarbunga-Holuhraun volcanotectonic episode in Iceland. J. Volcanol. Geotherm. Res. 308, 82–98. https://doi.org/10.1016/j.jvolgeores.2015.10.015

Chiu, Y.P., 1978. On the Stress Field and Surface Deformation in a Half Space With a Cuboidal Zone in Which Initial Strains Are Uniform. J. Appl. Mech. 45, 302. https://doi.org/10.1115/1.3424292

Dabrowski, M., Krotkiewski, M., Schmid, D.W., 2008. MILAMIN: MATLAB-based finite element method solver for large problems. Geochemistry, Geophys. Geosystems 9, 1–24. https://doi.org/10.1029/2007GC001719

Enami, M., Nishiyama, T., Mouri, T., 2007. Laser Raman microspectrometry of metamorphic quartz: A simple method for comparison of metamorphic pressures. Am. Mineral. 92, 1303–1315. https://doi.org/10.2138/am.2007.2438

Eshelby, J.D., 1957. The determination of the elastic field of an ellipsoidal inclusion, and related problems, in: Proceedings of the Royal Society of London A: Mathematical, Physical and Engineering Sciences. The Royal Society, pp. 376–396.

Fialko, Y., Khazan, Y., Simons, M., 2001. Deformation due to a pressurized horizontal circular crake in an elastic half-space, with application to volcano geodesy. Geophys. J. Int. 146, 181–190.

Galland, O., Holohan, E., van Wyk de Vries, B., Burchardt, S., 2015. Laboratory Modelling of Volcano Plumbing Systems: A Review, in: Physical Geology of Shallow Magmatic Systems. pp. 147–214. https://doi.org/10.1007/11157

Gerbault, M., Hassani, R., Novoa Lizama, C., Souche, A., 2018. Three-Dimensional Failure Patterns Around an Inflating Magmatic Chamber. Geochemistry, Geophys. Geosystems 19, 749–771. https://doi.org/10.1002/2017GC007174

Guldstrand, F., Galland, O., Hallot, E., Burchardt, S., 2018. Experimental Constraints on Forecasting the Location of Volcanic Eruptions from Pre-eruptive Surface Deformation.

Front. Earth Sci. 6, 1–9. https://doi.org/10.3389/feart.2018.00007

Kohn, M.J., 2014. “Thermoba-Raman-try”: Calibration of spectroscopic barometers and thermometers for mineral inclusions. Earth Planet. Sci. Lett. 388, 187–196. https://doi.org/10.1016/j.epsl.2013.11.054

Kouris, D.A., Mura, T., 1989. The elastic field of a hemispherical inhomogeneity at the free surface of an elastic half space. J. Mech. Phys. Solids 37, 365–379.

Lee, M., Jasiuk, I., Tsuchida, E., 1992. The sliding circular inclusion in an elastic half-plane 59, 57–64.

Mazzucchelli, M.L., Burnley, P., Angel, R.J., Morganti, S., Domeneghetti, M.C., Nestola, F., Alvaro, M., 2018. Elastic geothermobarometry: Corrections for the geometry of the host-inclusion system. Geology 1–4.

Mi, C., Kouris, D., 2013. Stress concentration around a nanovoid near the surface of an elastic half-space. Int. J. Solids Struct. 50, 2737–2748. https://doi.org/10.1016/j.ijsolstr.2013.04.029

Mi, C., Kouris, D.A., 2006. Nanoparticles Under the Influence of Surface/Interface elasticity. J. Mech. Mater. Struct. 1, 763–791.

Mindlin, R.D., Cheng, D.H., 1950. Thermoelastic Stress in the Semi-Infinite Solid. J. Appl. Phys. 931, 931–933. https://doi.org/10.1063/1.1699786

Mogi, K., 1958. Relations between the Eruptions of Various Volcanoes and the Deformations of the Ground Surfaces around them. Bull. Earthq. Res. Inst. 36, 99–134.

Morse, P.M., Feshbach, H., 1953. Methods of Theoretical Physics. McGraw-Hill.

Mura, T., 1987. Micromechanics of Defects in Solids. Springer Science & Business Media.

Mura, T., Jasiuk, I., Tsuchida, B., 1985. The stress field of a sliding inclusion. Int. J. Solids Struct. 21, 1165–1179. https://doi.org/10.1016/0020-7683(85)90002-2

Segall, P., 2005. Earthquake and Volcano deformation, Princeton University Press. https://doi.org/10.1002/0471743984.vse7429

Seo, K., Mura, T., 1979. The elastic field in a half space due to ellipsoidal inclusions with uniform dilatational eigenstrains. J. Appl. Mech. 46, 568–572. https://doi.org/10.1115/1.3424607

Thomas, J.B., Spear, F.S., 2018. Experimental study of quartz inclusions in garnet at pressures up to 3.0 GPa: evaluating validity of the quartz-in-garnet inclusion elastic thermobarometer. Contrib. to Mineral. Petrol. 173, 1–14. https://doi.org/10.1007/s00410-018-1469-y

Tsuchida, E., Nakahara, I., 1970. Three dimensional stress concentration around a spherical cavity in a semi infinite elastic body. Bull. Jpn. Soc. Mech 13, 499–508. https://doi.org/10.1248/cpb.37.3229

Zhang, Y., 1998. Mechanical and phase equilibria in inclusion-host systems. Earth Planet. Sci. Lett. 157, 209–222. https://doi.org/10.1016/S0012-821X(98)00036-3

Zhong, X., Moulas, E., Tajčmanová, L., 2018. Tiny timekeepers witnessing high-rate exhumation processes. Sci. Rep. 8, 2234. https://doi.org/10.1038/s41598-018-20291-7

## Appendix

The displacement in Cartesian coordinate can be expressed using displacement potentials as follow:

$$\begin{aligned} 2Gu_x &= \frac{\partial \Phi_0}{\partial x} + z\frac{\partial \Phi_3}{\partial x} \\ 2Gu_y &= \frac{\partial \Phi_0}{\partial y} + z\frac{\partial \Phi_3}{\partial y} \\ 2Gu_z &= \frac{\partial \Phi_0}{\partial z} + z\frac{\partial \Phi_3}{\partial z} - (3-4\nu)\Phi_3 \end{aligned} \tag{A1}$$

where $G$ is the shear modulus and $\nu$ is the Poisson ratio. These elastic moduli are chosen accordingly for mineral inclusion and host to compute the displacement for each object. For conciseness purpose, the overhead bar is not used here.

Strain and stress can be derived using the above displacement and transformed into any other coordinate systems. In spherical coordinate, the displacement and stress are given below.

$$\begin{aligned} 2Gu_R &= \frac{\partial \Phi_0}{\partial R} + \mu\left[R\frac{\partial \Phi_3}{\partial R} - (3-4\nu)\Phi_3\right] + 2Ge^* R P_0(\mu)\omega \\ 2Gu_\phi &= -\sin(\phi)\left[\frac{1}{R}\frac{\partial \Phi_0}{\partial \mu} + \mu\frac{\partial \Phi_3}{\partial \mu} - (3-4\nu)\Phi_3\right] \\ \sigma_{RR} &= \frac{\partial^2 \Phi_0}{\partial R^2} + \mu R\frac{\partial^2 \Phi_3}{\partial R^2} - 2(1-\nu)\mu\frac{\partial \Phi_3}{\partial R} - 2\nu\frac{1-\mu^2}{R}\frac{\partial \Phi_3}{\partial \mu} \end{aligned} \tag{A2}$$

$$\sigma_{\theta\theta} = \frac{1}{R}\frac{\partial\Phi_0}{\partial R} - \frac{\mu}{R^2}\frac{\partial\Phi_0}{\partial\mu} + (1-2\nu)\mu\frac{\partial\Phi_3}{\partial R} - \frac{1}{R}[2\nu + (1-2\nu)\mu^2]\frac{\partial\Phi_3}{\partial\mu}$$

$$\sigma_{\phi\phi} = -\frac{\partial^2\Phi_0}{\partial R^2} - \frac{1}{R}\frac{\partial\Phi_0}{\partial R} + \frac{\mu}{R^2}\frac{\partial\Phi_0}{\partial\mu} - \mu R\frac{\partial^2\Phi_3}{\partial R^2} - (1+2\nu)\mu\frac{\partial\Phi_3}{\partial R} + [1-(3-2\nu)(1-\mu^2)]\frac{1}{R}\frac{\partial\Phi_3}{\partial\mu}$$

$$\sigma_{\phi R} = \sin\phi\left[\frac{1}{R^2}\frac{\partial\Phi_0}{\partial\mu} - \frac{1}{R}\frac{\partial^2\Phi_0}{\partial\mu\partial R} + (1-2\nu)\frac{\partial\Phi_3}{\partial R} - \mu\frac{\partial^2\Phi_3}{\partial\mu\partial R} + 2(1-\nu)\frac{\mu}{R}\frac{\partial\Phi_3}{\partial\mu}\right]$$

where ω is zero for host, and one for inclusion. The rest displacement ($u_\theta$) and stress components ($\sigma_{\theta R}$, $\sigma_{\theta\phi}$) are zero due to the axisymmetric property of this problem.

In cylindrical coordinate, we have:

$$\begin{aligned}
u_r &= \frac{\partial\Phi_0}{\partial r} + z\frac{\partial\Phi_3}{\partial r}\\
u_z &= \frac{\partial\Phi_0}{\partial z} + z\frac{\partial\Phi_3}{\partial z} - (3-4\nu)\Phi_3\\
\sigma_{rr} &= \frac{\partial^2\Phi_0}{\partial r^2} + z\frac{\partial^2\Phi_3}{\partial r^2} - 2\nu\frac{\partial\Phi_3}{\partial z}\\
\sigma_{zz} &= \frac{\partial^2\Phi_0}{\partial z^2} - 2(1-\nu)\frac{\partial\Phi_3}{\partial z} + z\frac{\partial^2\Phi_3}{\partial z^2}\\
\sigma_{rz} &= \frac{\partial^2\Phi_0}{\partial z\partial r} - (1-2\nu)\frac{\partial\Phi_3}{\partial r} + z\frac{\partial^2\Phi_3}{\partial z\partial r}\\
\sigma_{\theta\theta} &= \frac{1}{r}\frac{\partial\Phi_0}{\partial r} + \frac{z}{r}\frac{\partial\Phi_3}{\partial r} - 2\nu\frac{\partial\Phi_3}{\partial z}
\end{aligned} \tag{A3}$$

For the coordinate transformation of the displacement potentials, the following mathematical rules are needed (see e.g. Morse and Feshbach, 1953; Tsuchida and Nakahara, 1970):

$$\frac{P_n(\mu)}{R^{n+1}} = \frac{(-1)^n}{n!}\int_0^\infty \lambda^n J_0(\lambda r)e^{\lambda z}d\lambda \tag{A4}$$

where $z < 0$, and:

$$J_0(\lambda r)e^{-\lambda z} = \sum_{n=0}^{\infty}(-1)^n\frac{(\lambda R)^n}{n!}P_n(\mu) \tag{A5}$$

This transformation is valid only when $R \sim 1$, thus it is particularly suitable for matching the traction at inclusion-host interface due to the choice of inclusion radius as one.

For Legendre polynomials, the following recurrence relations can be useful in deriving the stress and displacement in Eq. 14 and 16:

$$\begin{aligned}
\mu P_n(\mu) &= \frac{n+1}{2n+1}P_{n+1}(\mu) + \frac{n}{2n+1}P_{n-1}(\mu)\\
\mu P_n'(\mu) &= \frac{n}{2n+1}P_{n+1}'(\mu) + \frac{n+1}{2n+1}P_{n-1}'(\mu)\\
P_n(\mu) &= \frac{1}{2n+1}[P_{n+1}'(\mu) - P_{n-1}'(\mu)]\\
\frac{\mu^2-1}{n}P_n'(\mu) &= \frac{n+1}{2n+1}[P_{n+1}(\mu) - P_{n-1}(\mu)]
\end{aligned} \tag{A6}$$

The derivative of Bessel function has some useful properties that have been taken advantaged of during the derivation for displacement and stress in Eq. 21 and 23.

$$\frac{\partial J_0(\lambda r)}{\partial r} = -\lambda\, J_1(\lambda r) \tag{A7}$$

$$\frac{\partial^2 J_0(\lambda r)}{\partial r^2} = -\lambda^2 J_0(\lambda r) + \frac{\lambda}{r} J_1(\lambda r)$$